

Beam characterization for the QUIET Q-Band instrument using polarized and unpolarized astronomical sources

Raul A. Monsalve^a for the QUIET Collaboration

^aDept. of Physics, U. of Miami, 1320 Campo Sano Drive, Coral Gables, USA 33146

ABSTRACT

Beam characterization is of critical importance when analyzing and interpreting data from Cosmic Microwave Background (CMB) experiments. In this paper we present scanning strategies, data analysis methods and results of the 44 GHz (Q-Band) beam characterization for the Q/U Imaging Experiment (QUIET) Phase-I, using the Crab nebula (Tau A) and Jupiter as polarized and unpolarized point sources, respectively. The beams are modeled as a sum of gaussian terms multiplied by orthogonal polynomials after symmetrization using observations taken at different rotation angles about the optical axis. The ℓ -space window function calculation procedure is explained and applied, along with the corresponding propagation of parameter uncertainty. These window functions encode the effect of the finite resolution of the instrument on its ability to measure the angular power spectrum, as a function of multipole ℓ . Additionally, the instrumental polarization is characterized in terms of two-dimensional Mueller fields which describe the coupling of the Stokes parameters. The data presented in this work were collected during the first season of QUIET observations that started in October 2008.

Keywords: cosmic microwave background, polarization, observations, methods: numerical

1. INTRODUCTION

The primary scientific motivation of QUIET is to make precision measurements of the CMB polarization with the ultimate goal of detecting in it patterns imprinted by gravitational waves from a primordial epoch of inflation. The polarization can be separated into E-modes and B-modes based on symmetry properties;^{1–3} the B-modes at large angles only arise from gravity waves. All of these signals are very faint and require a combination of an extremely sensitive detector system and exquisite control and/or characterization of systematic effects.

The QUIET receivers measure simultaneously the Q and U Stokes linear polarization parameters of the CMB, as well as its temperature anisotropies. QUIET consists of two phases; Phase-I is currently ongoing and has carried out observations at 44 GHz (Q-Band) and 95 GHz (W-Band), while Phase-II is being developed and expected to continue and improve Phase-I results. Hereafter QUIET refers to QUIET Phase-I unless otherwise noted.

In this paper we describe the measurement of the 44 GHz beam shapes and characterization of the corresponding window functions for both the total power (temperature) and polarization beams. The measurements and characterization of the 95 GHz system are underway and will follow the general procedure outlined below. Other papers in these proceedings provide an overview of the QUIET instrument,⁴ the QUIET polarization modules⁵ and the responsivity characterization.⁶

2. OPTICAL DESIGN

The QUIET optical design incorporates a side-fed Dragonian antenna⁷ which uses a 1.4 m paraboloidal primary mirror and concave hyperboloidal secondary mirror, Figure 1 (left). These combine to generate a wide field of view with excellent polarization characteristics and minimal beam distortion. The Q-Band receiver, which operated during the first season of Phase-I, consists of 19 module elements from which two are dedicated to measurement of CMB temperature anisotropies and all the rest to polarization detection. The W-Band receiver, currently being used, has a total of 90 module elements out of which six are dedicated to temperature. In

Send correspondence to raul@physics.miami.edu

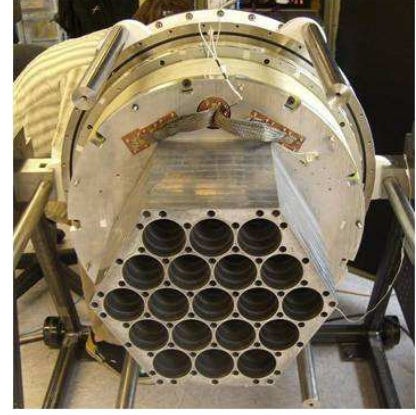


Figure 1. **Left:** Dragonian antenna during assembly tests. It uses a 1.4 m paraboloidal primary and concave hyperboloidal secondary aluminum mirrors. The Q-Band receiver was also installed during this test, visible on the right under the flag. The primary is facing upward. **Right:** Q-Band corrugated feedhorn platelet array. The horns corresponding to the TT modules are in the lowest row; horn 17 is at the center of the row and horn 18 is at the right corner.

both cases, polarization and temperature modules have four readout channels, Q1, Q2, U1 and U2 nominally measuring $+Q$, $-Q$, $-U$ and $+U$.

The first block in the receiver corresponds to a corrugated feedhorn array, Figure 1 (right), that couples the radiation coming from the antenna to a septum polarizer⁸ which splits the left and right circular polarizations before they are fed into the polarimeter modules.⁵ Corrugated feeds offer the combination of broad bandwidth and low cross polarization necessary to minimize the systematic effects that can be introduced by instrumental polarization. They also provide symmetric beams with low sidelobes, resulting in minimal spillover. Since standard electroformed corrugated feeds are prohibitively expensive, a low cost option using platelet arrays* of corrugated feedhorns was used.⁹ QUIET is the first CMB experiment to use either the side-fed Dragonian antenna or platelet arrays. Pictures of the antenna and Q-Band platelet array are shown in Figure 1. Large absorbing ground shields,⁴ which were installed once the antenna was placed on its three-axis mount, are not shown in this figure.

3. OBSERVATIONS AND PRELIMINARY DATA REDUCTION

3.1 JUPITER

Jupiter is used as a beam mapping and calibration source for the two temperature modules (hereafter TT modules) of the Q-band array. It was observed with azimuth scans at constant elevation with an amplitude (half amplitude) between 3° and 6° .

The TT modules output temperature differences such as $T_{17}^a - T_{18}^b$, where the subscripts denote two feedhorns, separated on the sky by 1.75° , and the superscripts denote two orthogonal linear polarization states from those feedhorns. Module 17 outputs both $T_{17}^a - T_{18}^b$ and $T_{18}^b - T_{17}^a$, on the detectors Q1 and Q2. Module 18 outputs $T_{17}^b - T_{18}^a$ and its negative. Thus each observation of Jupiter results in eight beam maps from two feedhorns at the edge of the array, as seen in Figure 1 (right).

Figure 2 shows a section of a raw map from detector Q1 of module 18 in *instrumental coordinates* (x, y) for a single observation. These coordinates represent angular distances on the sky with the origin at the location of the beam for the horn being analyzed, such that x is parallel to the row of feedhorns as seen in Figure 1 (right). It is easy to observe in Figure 2 the differential beam patterns corresponding to horns 17 and 18 respectively.

For the analysis presented here we use a total of 10.8 hours of data taken during the first season of the experiment, not including one compromised by bad weather conditions. When analyzing these observations

*Platelet arrays comprise layers of plates bonded together, each machined with one to several of the corrugations for each of the elements of the array.

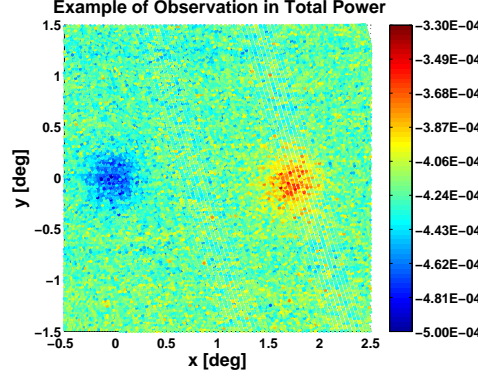


Figure 2. This figure shows the resulting double beam map when observing Jupiter with the TT modules.

individually it is necessary to remove their signal baseline in order to compensate for the $1/f$ noise from the receiver and atmosphere, that however small, could bias the final results. The most practical way of doing it is by pre-pixelizing the raw map with a convenient resolution of $0.03^\circ \times 0.03^\circ$, blanking out the region where the beams lie up to a radius of 0.75° , or 3.75 times the expected gaussian width of the beam (beam width hereafter), and calculating the mean signal offset at each y -step, which is then removed. The data are coadded in instrumental coordinates after applying the gain model discussed in Dumoulin et al. (2010).⁶ Finally the amplitude of each map is normalized to unity, leaving them ready for the analysis of Section 4.

3.2 CRAB NEBULA

Tau A (Crab Nebula) is the brightest polarized extrasolar radio source, and is therefore broadly used as calibrator by CMB experiments.¹⁰ It was scanned with purposes of responsivity calibration, polarization angle identification and beam characterization for the polarization detectors. The analysis presented here focuses on beam characterization for the central horn of the array since most of the observations concentrated on this horn. Additional measurements were performed on other horns to check predicted trends in critical beam parameters.

The data considered in the analysis correspond to observations taken between November 2008 and May 2009 that amount to 18 hours of raster scans carried out at different rotation angles about the optical axis, or *boresight orientations*, with amplitude of approximately 0.9° on the sky. For every observation, the baseline offset is eliminated by fitting and removing a y -dependent plane, after blanking out the area where the beam is located up to a radius of 0.75° , as in the Jupiter case. The gain model from Dumoulin et al. is applied to the data which are then concatenated and binned in instrumental coordinates with pixel size of $0.03^\circ \times 0.03^\circ$. The most important aspect of this pixelization is that due to the scanning strategy, within each pixel centered at \hat{n} we have data points taken at different angles η , which incorporates the parallactic angle of the measurement, the boresight orientation angle and the polarization angle of the detectors as established from measurements of the Moon. The response of the Q and U detectors can then be described in the following way:

$$\begin{aligned} Q(\hat{n}, \eta) &= R \cdot \Gamma \cdot I_{src} \{m_{QI}(\hat{n}) + p \cdot m_{QQ}(\hat{n}) \cdot \cos(2[\gamma_{PA} - \eta]) + p \cdot m_{QU}(\hat{n}) \cdot \sin(2[\gamma_{PA} - \eta])\} \\ U(\hat{n}, \eta) &= R \cdot \Gamma \cdot I_{src} \{m_{UI}(\hat{n}) + p \cdot m_{UU}(\hat{n}) \cdot \sin(2[\gamma_{PA} - \eta]) + p \cdot m_{UQ}(\hat{n}) \cdot \cos(2[\gamma_{PA} - \eta])\} \end{aligned} \quad (1)$$

where R is the responsivity of the receiver⁶ [$V K^{-1}$], Γ is the telescope sensitivity [$K Jy^{-1}$], $I_{src}=317.7$ [Jy] is the flux density of Tau A from Wieland et al. (2010),¹⁰ $\gamma_{PA}=150.7^\circ$ is the position angle of Tau A¹⁰ and $p=0.0697$ is the polarization fraction of Tau A.¹⁰ We thus obtain simultaneously the value of the two-dimensional Mueller fields at position \hat{n} from a linear least squares fit. The m_{QI} Mueller field represents the coupling of the sky Stokes parameter I into the measured Q.^{11,12} The definition of the other Mueller fields is analogous.

The Mueller fields are related to various combinations of the co- and cross-polar, E- and H-plane beam patterns.¹² The characterization of these maps is carried out differently for the polarization beams (contained

in m_{QQ} and m_{UU}) and the leakage beams (m_{QI} , m_{UI} , m_{QU} and m_{UQ}) due to the nature of the information we want to extract. In the first case we are interested in parameters such as beam elongation, rotation angle, axially symmetric profile and window function, whereas for the leakage beams a two-dimensional shapelet¹³ modeling is of particular interest, in order to quantify the relative contribution of the monopole, dipole and quadrupole term to the beam distortions.¹⁴

The m_{QI} and m_{UI} fields are of particular concern to precision CMB polarization measurements because they can give rise to a false polarization signal, while the m_{QU} and m_{UQ} fields can change the nominal instrument polarization axis that is fixed by the septum polarizer.

4. TOTAL POWER BEAMS AND WINDOW FUNCTIONS

The beams contained in the final normalized maps of Section 3.1 are modeled as two-dimensional elliptic gaussians oriented at any angle. We define a coordinate system with axes $(\hat{\mu}, \hat{\nu})$ fixed to the ellipse such that its semimajor axis is aligned with $\hat{\mu}$, and free to rotate an angle χ counterclockwise from $+\hat{x}$, the positive half of the horizontal axis in instrumental coordinates. In these rotated coordinates we define the beam widths σ_μ and σ_ν , where clearly $\sigma_\mu \geq \sigma_\nu$. The two-dimensional elliptic beam model is therefore:

$$b_{2d}(x, y) = \exp \left(-\frac{1}{2\sigma_\mu^2} [x \cos \chi + y \sin \chi]^2 - \frac{1}{2\sigma_\nu^2} [-x \sin \chi + y \cos \chi]^2 \right). \quad (2)$$

This model serves us primarily to quantify the elongation and rotation angle of the beams and check their consistency. The elongation, defined here as $\epsilon = \frac{(\sigma_\mu - \sigma_\nu)}{(\sigma_\mu + \sigma_\nu)} \times 100\%$, is expected to be low in every case, and given our CMB scanning strategy that includes natural sky rotation as well as artificial telescope boresight rotation, it is appropriate to describe the beam as a one-dimensional axially symmetric profile, whose main parameter is a single effective beamsize.¹⁵ Defining the normalized temperature beam map in polar coordinates as $T(\theta, \phi)$, where θ and ϕ are the distance from the beam center and the polar angle respectively, the expression to compute the symmetric profiles is:¹⁶

$$b_s^d(\theta) = \frac{\int d\phi' T(\theta, \phi')}{\int d\phi'}. \quad (3)$$

This symmetric beam is modeled as a series expansion of Gauss-Hermite functions, a particular one-dimensional application of the shapelet decomposition method,¹³ with the equation

$$b_s^m(\theta) = \exp \left(-\frac{\theta^2}{2\sigma_s^2} \right) \sum_{i=0}^{m_h} a_{2i} H_{2i} \left(\frac{\theta}{\sigma_s} \right) \quad (4)$$

where σ_s is the symmetric gaussian beam size and H_{2i} is the Hermite polynomial of order $2i$. This expansion is needed in order to parameterize the deviations from gaussianity of the beam, that appear significantly beyond an angular distance of two times the expected beamsize, or 0.4° in this case. From shapelet theory we know that there is not a unique value of σ_s (in general called *scale size*) that best describes the data using Equation 4, as long as the chosen one is within a reasonable range.¹⁷⁻¹⁹ We choose σ_s as the gaussian beam width of the main lobe by fitting with $m_h = 0$ for angles $|\theta| < 0.4^\circ$. Note that we only use even Hermite functions in the expansion since we are assuming a symmetric beam.

With this beam profile model we approach the window function calculation procedure following the outline found in Page et al. (2003),¹⁵ where the Legendre transform of the beam, b_ℓ , is related to the window function by $w_\ell = b_\ell^2$. This transform is defined as

$$b_\ell = \frac{2\pi}{\Omega_B} \int b_s^m(\theta) P_\ell(\cos \theta) d(\cos \theta) \equiv \frac{B_\ell}{\Omega_B} \quad (5)$$

where P_ℓ corresponds to the Legendre polynomial of degree ℓ and Ω_B is the main beam solid angle. We can simplify the integration by writing

Table 1. Basic beam and telescope parameters obtained from the TT channels using Jupiter as calibration source. The eight cases are classified by *module*, *horn* and *detector*. The values presented are beam elongation ϵ , rotation angle χ , symmetric FWHM, integrated main beam solid angle Ω_B , telescope gain G_m and conversion factor Γ . The errors quoted here do not explicitly account for uncertainties in the gain or pointing model.

	ϵ [%]		χ [deg]		FWHM [deg]		Ω_B [μ sr]	G_m [dBi]	Γ [μ K Jy $^{-1}$]
	value	error	value	error	value	error			
m17/h17/Q1	1.5	0.3	86	6	0.460	0.002	80.7	51.9	208.6
m17/h17/Q2	1.6	0.3	83	6	0.456	0.002	79.5	52.0	211.8
m17/h18/Q1	2.3	0.3	90	4	0.457	0.002	78.6	52.0	214.2
m17/h18/Q2	1.4	0.3	89	6	0.457	0.002	78.3	52.1	215.1
m18/h17/Q1	0.6	0.3	77	14	0.450	0.002	77.4	52.1	217.6
m18/h17/Q2	0.7	0.3	46	12	0.453	0.002	78.0	52.1	215.9
m18/h18/Q1	1.2	0.3	85	7	0.460	0.002	79.8	52.0	210.9
m18/h18/Q2	1.7	0.3	93	5	0.460	0.002	80.4	51.9	209.4

$$B_\ell = \sum_{i=0}^{m_h} a_{2i} B_{\ell i}, \quad (6)$$

where

$$B_{\ell i} = 2\pi \int_0^\pi e^{-\frac{\theta^2}{2\sigma_s^2}} H_{2i} \left(\frac{\theta}{\sigma_s} \right) P_\ell(\cos \theta) \sin \theta d\theta. \quad (7)$$

This last integration is carried out for each expansion term ($i = 0, 1, \dots, m_h$) up to a value of $\ell = 700$, sufficiently higher than our sensitivity range, which is about 25-400 for Phase-I Q-band. Finally we calculate the linear combination of Equation (6) using the Hermite coefficients extracted previously, and the transfer function is obtained using the normalization $b_\ell = B_\ell / B_{\ell=0}$.

The fractional uncertainties in the window functions are related to the ones in the transfer functions b_ℓ by $\Delta w_\ell / w_\ell = 2\Delta b_\ell / b_\ell$, so it is necessary to calculate Δb_ℓ by propagating the uncertainties from the covariance matrix of the Hermite coefficients, $C_{ij}^{aa'}$, using

$$\Sigma_{\ell\ell'}^B = \sum_{i,j=0}^{m_h} B_{\ell i} C_{ij}^{aa'} B_{\ell' j}, \quad (8)$$

which allows us to write the covariance matrix of the transfer function b_ℓ as

$$\Sigma_{\ell\ell'}^b = \sum_{i,j=0}^{m_h} \frac{\partial b_\ell}{\partial a_{2i}} C_{ij}^{aa'} \frac{\partial b_{\ell'}}{\partial a_{2j}} = \frac{1}{(B_{\ell=0})^2} (\Sigma_{\ell\ell'}^B + b_\ell b_{\ell'} \Sigma_{00}^B - b_\ell \Sigma_{0\ell'}^B - b_{\ell'} \Sigma_{\ell 0}^B), \quad (9)$$

from where we finally get $\Delta b_\ell = (\Sigma_{\ell\ell}^b)^{\frac{1}{2}}$, the diagonal elements plotted in Figures 3 and 4.

The a_{2i} coefficients and their covariance matrix are computed using the least squares minimization method. To find out how many terms to use in the Gauss-Hermite expansion we carry out a reduced- χ^2 comparison, where the effect on the goodness of fit of the inclusion of every additional term is quantified. Even though $m_h=6$ noticeably improves the reduced- χ^2 compared to the pure gaussian case ($m_h=0$), we decide to use $m_h=10$ since at that level the trend has been settled for both, the present total power profiles and the polarization profiles analyzed next. Therefore, the orders of the Hermite polynomials in the symmetric beam model of Equation 4 are 0, 2, 4,...20, eleven terms total.

With all these specifications we carry out the analysis and obtain the results presented in Table 1 and Figure 3. From the table we see that the beam elongation has an average value of 1.4%, and the associated rotation angles indicate that the beams are consistently aligned almost vertically, except for the cases with the smallest ellipticity where the uncertainty of the angle is correspondingly higher, in particular the m18/h17/Q2 case that with a

Table 2. Basic beam and telescope parameters extracted from the m_{QQ} and m_{UU} Mueller maps using Tau A as calibration source, for the Q and U detectors of the central polarization module. The values presented are beam elongation ϵ , rotation angle χ , symmetric FWHM, integrated main beam solid angle Ω_B , telescope gain G_m and conversion factor Γ . The errors quoted here do not explicitly account for uncertainties in the gain or pointing model.

	ϵ [%]		χ [deg]		FWHM [deg]		Ω_B [μ sr]	G_m [dBi]	Γ [μ K Jy $^{-1}$]
	value	error	value	error	value	error			
Q	2.0	0.6	125	9	0.448	0.003	73.7	52.3	228.4
U	1.0	0.6	58	16	0.456	0.004	70.4	52.5	239.3

rotation angle of $46 \pm 12^\circ$ lies outside the trend presented by the seven other cases but has an elongation of 0.7%. The table additionally shows the FWHM of the symmetrized beam, defined as $\text{FWHM} = \sqrt{8 \ln 2} \sigma_s$, the beam solid angle Ω_B obtained by integrating the final Jupiter maps up to $\theta = 0.9^\circ$, the telescope gain $G_m = 10 \log_{10} \left(\frac{4\pi}{\Omega_B} \right)$ and the conversion factor depending on the calculated solid angles

$$\Gamma \left[\frac{\mu\text{K}}{\text{Jy}} \right] = \frac{10^{-20} c^2}{2k_b \nu_e^2 \Omega_B}, \quad (10)$$

where $\nu_e = 44$ GHz corresponds to the effective observing frequency.

5. POLARIZATION BEAMS AND WINDOW FUNCTIONS

5.1 Polarization Beams

In this section we carry out the same procedure that the one used in the total power case to analyze the main beams contained in the two-dimensional m_{QQ} and m_{UU} Mueller maps obtained from Equations 1 and the axially symmetric profiles generated from them, so there is no need for further development. The same beam models apply, as well as the window function calculation method, obtaining the results of Table 2. The profiles and window functions are presented in Figure 4, and the fitted two-dimensional beams are shown as contour plots in Figure 6 (first column), along with the leakage maps explained next. The Q and U data we use in this section corresponds to the detector pair (Q1,U1). Similar results are obtained when (Q2,U2) are used.

5.2 Leakage Beams

Non-idealities in the instrument can produce a leakage of the total intensity into the polarization signals causing CMB temperature anisotropy to leak into the polarization, an effect defined as I \rightarrow Q/U leakage. Similarly, non-idealities in the instrument can rotate its polarization axis away from the nominal axis set by the septum polarizer giving rise to Q \leftrightarrow U leakage. These effects can be quantified by the previously described Mueller leakage beams m_{QI} , m_{UI} , m_{QU} and m_{UQ} , which therefore need to be properly characterized.

For this purpose we model the data with a two-dimensional shapelet expansion in terms of Gauss-Hermite functions in cartesian coordinates, equivalent to the one-dimensional model used for the symmetrized beam profiles. In this case however, since there are no parity requirements for the basis functions, i.e., they do not need to be symmetric about $x=0$ or $y=0$, it is possible to use all the desired consecutive integers in the expansion. Just like in the one-dimensional case, the scale size is chosen to be the size of the main beam obtained from the axially symmetric profile presented in Table 2, implying that the whole set of extracted coefficients is only meaningful under those conditions.

The normalized basis functions are defined as:

$$f_{i,j}(x,y) = [2^{i+j} \pi i! j! \sigma_s^2]^{-\frac{1}{2}} H_i \left(\frac{x}{\sigma_s} \right) H_j \left(\frac{y}{\sigma_s} \right) e^{-\frac{1}{2\sigma_s^2}(x^2+y^2)}, \quad (11)$$

but it is more convenient if we simplify the nomenclature defining:

Table 3. Expansion coefficients of Equation 13 and their uncertainties.

	m_{QI} $\times 10^{-3}$	error $\times 10^{-3}$	m_{UI} $\times 10^{-3}$	error $\times 10^{-3}$	m_{QU} $\times 10^{-3}$	error $\times 10^{-3}$	m_{UQ} $\times 10^{-3}$	error $\times 10^{-3}$
d_1	-2.4	0.1	0.9	0.1	26	2	-27	2
d_2	0.7	0.1	0.6	0.1	-7	2	4	2
d_3	0.04	0.1	-0.09	0.1	-2	2	1	2
d_4	-0.6	0.1	0.02	0.1	-4	2	-5	2
d_5	0.7	0.1	-0.4	0.1	3	2	-4	2
d_6	0.2	0.1	-0.4	0.1	2	2	-3	2

$$\begin{aligned}
\Psi_1 &= f_{0,0}, \Psi_4 = f_{1,0} \\
\Psi_2 &= f_{0,1}, \Psi_5 = f_{2,0} \\
\Psi_3 &= f_{0,2}, \Psi_6 = f_{1,1}.
\end{aligned} \tag{12}$$

The number of expansion terms is chosen to be six since this set includes all the critical terms that we want to examine, and also because beyond that value the χ^2 does not improve noticeably. With this formulation we write the leakage beam model as:

$$b_{leak}(x, y) = \sum_{i=1}^6 d_i \Psi_i(x, y). \tag{13}$$

The d_i coefficients are computed taking advantage of the orthonormality between the basis functions, and the calculation of their covariance assumes white uncorrelated noise. They are therefore given by:

$$\begin{aligned}
d_i &= \int M(x, y) \Psi_i(x, y) dx dy \\
C_{ij}^{dd'} &= \int [N(x, y)]^2 \Psi_i(x, y) \Psi_j(x, y) dx dy
\end{aligned} \tag{14}$$

where M represents the leakage map under analysis (m_{QI} , m_{UQ} , etc.) and N corresponds to its associated map of uncertainties. Finally, in order to derive the errors in the coefficients from the covariance matrix $C_{ij}^{dd'}$ we follow the parameter estimation and marginalization procedure outlined in Huffenberger et al. (2004).²⁰

The results are summarized in Table 3, where cases with $|d_i| \geq 3\sigma_{d_i}$ are shown in bold font, stressing the statistically significant terms in the series. The normalized basis functions corresponding to each term in the expansion are shown in Figure 5 and the leakage beams reconstructed using the coefficients of the table are presented in Figure 6 along with the previously described polarization beams. The reduced- χ^2 obtained when comparing the original and reconstructed leakage beam maps are 1.15, 1.06, 1.11 and 1.09 for m_{QI} , m_{UI} , m_{QU} and m_{UQ} respectively.

6. DISCUSSION

6.1 Main Beams

Tables 1 and 2 show the parameters corresponding to the total power and polarization main beams. All the total power cases have a small beam elongation, with an average of 1.4%, that allows symmetrization, and the beams are consistently aligned vertically except for the m18/h17/Q2 case that has the second lowest elongation, 0.7%. The symmetrized FWHM is also consistent among the cases with an average of 0.456° and a sample standard deviation of 0.0036° , 1.8 times larger than the uncertainties.

The main beam solid angles calculated from the co-added maps show a sample standard deviation of 1.19 [μsr] whose origin, given the FWHM values, has to lie in the differences that occur below the -10 dB level where

the non-gaussianity arises. This can be checked by comparing the fitted linear coefficients of the one-dimensional Gauss-Hermite expansion between all the cases.

In the polarization case, the beams have an elongation consistent with the total power beams but the rotation angles are different, since as expected, the m_{QQ} and m_{UU} beams are oriented perpendicular to each other, i.e., there is an angle of 90° between them, to within the uncertainties. The FWHM of the m_{QQ} beam is 2% smaller than the average total power value, and m_{UU} is practically equal to that average. However, the noticeable difference between the polarization and total power beams is their solid angle values. For Q it is 6.8% smaller and for U it is 10.9% smaller than the average total power case. Given the small differences in FWHM, it is evident that the non-gaussian region of the polarization beams is driving the solid angle difference. As it can be seen from Figures 3 (left) and 4 (left), the total power profile shows that the beam departs from gaussianity at ≈ -10 dB whereas the profile of m_{QQ} does it at ≈ -14 dB, difference then reflected in the solid angle calculation. The uncertainty propagation for the solid angles is still under study, so definitive statements about their consistency cannot be made at this point.

6.2 Polarization Leakage Beams

For the m_{QI} and m_{UI} Mueller fields we are interested in quantifying the contribution from quadrupole terms since they could induce a coupling to the local CMB anisotropy generating spurious polarization. From Equations 12 and Figure 5 we see that these terms can be represented directly by d_6 or by a combination of d_3 and d_5 (quadrupole rotated by 45°). Table 3 shows that d_3 has no significance in either map implying that the spurious polarization originated from a rotated quadrupole is expected to be highly suppressed. The non-rotated case appears significantly only in m_{UI} , with $|d_6| > 3\sigma_{d_6}$. Future work will make use of the reconstructed m_{QI} and m_{UI} beams in combination with WMAP temperature data in order to generate leakage maps and assess the effect of instrumental polarization on our final CMB and galactic plane results. Finally we introduce the *fractional instrumental polarization*, a practical quantity for comparing leakage content, defined as

$$f_{QI} = \frac{\int |m_{QI}| d\Omega}{\int m_{QQ} d\Omega}, \quad f_{UI} = \frac{\int |m_{UI}| d\Omega}{\int m_{UU} d\Omega}, \quad (15)$$

where the integrals $\int |m_{QI}| d\Omega$ and $\int |m_{UI}| d\Omega$ were calculated using the reconstructed leakage beams and the quantities in the denominator are the previously defined polarization beam solid angles Ω_B for Q and U presented in Table 2. The resulting values are $100\% \times f_{IQ} = 0.6\%$ and $100\% \times f_{IU} = 0.35\%$. These results are comparable to I \rightarrow Q/U values determined during the analysis of skydip data.⁶

The relatively large m_{QU} and m_{UQ} fields determined in this analysis are due to a known offset between the nominal instrument polarization angles as measured with the Moon and those measured with Tau A. Given that the ratios between those leakages and the polarization beams are $|m_{QU}|/m_{QQ} \approx |m_{UQ}|/m_{UU} \leq 0.07$, as can be easily checked from Figure 6, we find an upper bound for this detector angle phase shift of $\frac{1}{2} \tan^{-1}(0.07) \approx 2^\circ$ in both cases.

ACKNOWLEDGMENTS

Support for the QUIET instrument and operations comes through the NSF cooperative agreement AST-0506648. Support also provided by AST-04-49809, DE-AC02-05CH11231, JSPS KAKENHI (A) 20244041, NSF PHY-0355328 and by the Strategic Alliance for the Implementation of New Technologies (SAINT). We are particularly indebted to the engineers who maintained and operated the telescope: J. Cortes, C. Jara, F. Munoz, and C. Verdugo.

REFERENCES

- [1] Hu, W. and White, M., “CMB Anisotropies: Total Angular Momentum Method,” *Physical Review D* **56-2**, 596–615 (1997).
- [2] Kovac, J., Leitch, E. M., and Pryke, C., “Detection of polarization in the cosmic microwave background using DASI,” *Nature* **420**, 772–786 (2002).
- [3] Readhead, A., Myers, S. T., and Pearson, T. J., “Polarization Observations with the Cosmic Background Imager,” *Science* **306-5697**, 836–844 (2004).
- [4] Buder, I., “Q/U Imaging Experiment (QUIET): a ground-based probe of cosmic microwave background polarization,” *Proc. SPIE (to appear)* **7741** (2010).
- [5] Cleary, K., “Coherent polarimeter modules for the QUIET experiment,” *Proc. SPIE (to appear)* **7741** (2010).
- [6] Dumoulin, R., “Responsivity Calibration of the Quiet Q-band Array,” *Proc. SPIE (to appear)* **7741** (2010).
- [7] Hanany, S. and Marrone, D., “Comparison of designs of off-axis gregorian telescopes for millimeter-wave large focal-plane arrays,” *Applied Optics* **41**, 4666–4670 (2002).
- [8] Bornemann, J. and Labay, V., “Ridge waveguide polarizer with finite and stepped-thickness septum,” *IEEE Trans. Microwave Theory Tech.* **43**, 1782–1787 (1995).
- [9] Gundersen, J. and Wollack, E., “Millimeter-wave Corrugated Platelet Feeds,” *Journal of Physics: Conference Series* **155** (2009).
- [10] Weiland, J., Odegard, N., and Hill, R., “Seven-Year Wilkinson Microwave Anisotropy Probe (WMAP) Observations: Planets and Celestial Calibration Sources,” **arXiv:1001.4731** (2010).
- [11] Heiles, C., “A Heuristic Introduction to Radioastronomical Polarization,” *Single-Dish Radio Astronomy: Techniques and Applications, ASP Conference Proceedings* **278**, 131–152 (2002).
- [12] O’Dea, D., Challinor, A., and Johnson, B., “Systematic Errors in Cosmic Microwave Background Polarization Measurements,” *Monthly Notices of the Royal Astronomical Society* **376**, 1767–1783 (2007).
- [13] Refregier, A., “Shapelets: I. A Method for Image Analysis,” *Monthly Notices of the Royal Astronomical Society* **338-1**, 35–47 (2002).
- [14] Hu, W., Hedman, M., and Zaldarriaga, M., “Benchmark parameters for CMB polarization experiments,” *Physical Review D* **67**, 043004 (2003).
- [15] Page, L., Barnes, C., and Hinshaw, G., “First-Year Wilkinson Microwave Anisotropy Probe (WMAP) Observations: Beam Profiles and Window Functions,” *The Astrophysical Journal Supplement Series* **148**, 39–50 (2003).
- [16] Hincks, A., Acquaviva, V., and Ade, P., “The Atacama Cosmology Telescope (ACT): Beam Profiles and First SZ Cluster Maps,” *ApJ (submitted)* (2009).
- [17] Berry, R., Hobson, M. P., and Withington, S., “Modal Decomposition of Astronomical Images with Application to Shapelets,” *Monthly Notices of the Royal Astronomical Society* **354**, 199–211 (2002).
- [18] Melchior, P., Meneghetti, M., and Bartelmann, M., “Reliable Shapelet Image Analysis,” *Astronomy and Astrophysics* **463**, 1215–1225 (2007).
- [19] Refregier, A., Chang, T., and Bacon, D., “Shapelets: A New Method to Measure Galaxy Shapes,” *Proceedings of the Yale Cosmology Workshop*, 29–38 (2001).
- [20] Hufenberger, K., Seljak, U., and Makarov, A., “Sunyaev-Zeldovich Effect in WMAP and its Effect on Cosmological Parameters,” *Phys. Rev. D* **70**, 063002 (2004).

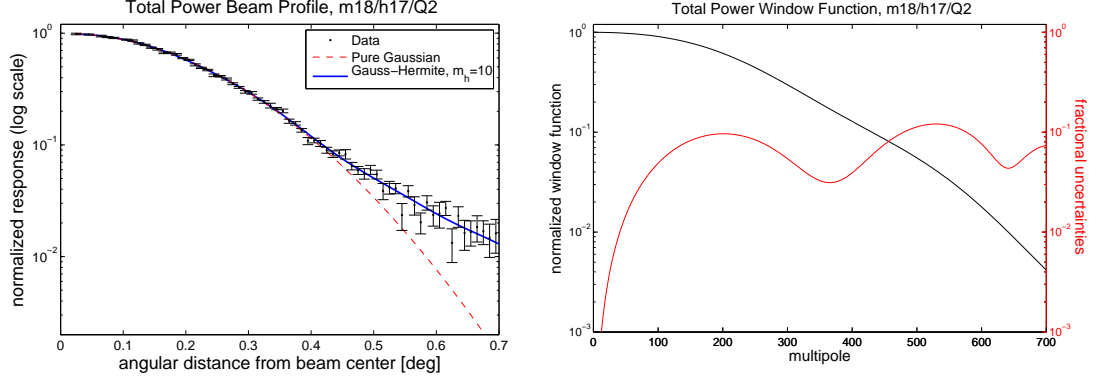


Figure 3. **Left:** Representative total power beam profile, from module 18, horn 17, detector Q2. The simpler pure gaussian model is contrasted with the more accurate Gauss-Hermite series, presented in Equation 4. **Right:** Window function w_ℓ and fractional uncertainties $\Delta w_\ell/w_\ell$ for the same case. The results for the other cases are almost identical.

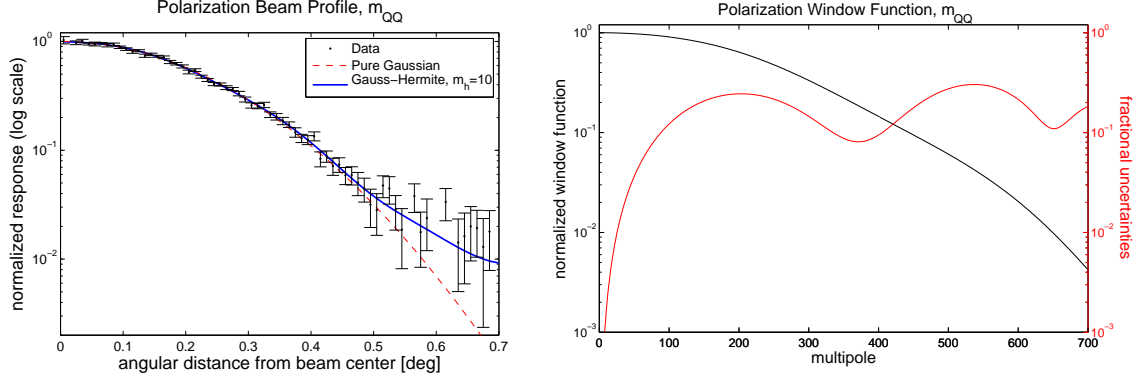


Figure 4. **Left:** Representative polarization beam profile, from the central module 09, detector Q. **Right:** Window function w_ℓ and fractional uncertainties $\Delta w_\ell/w_\ell$ for the same case. The results for U are equivalent.

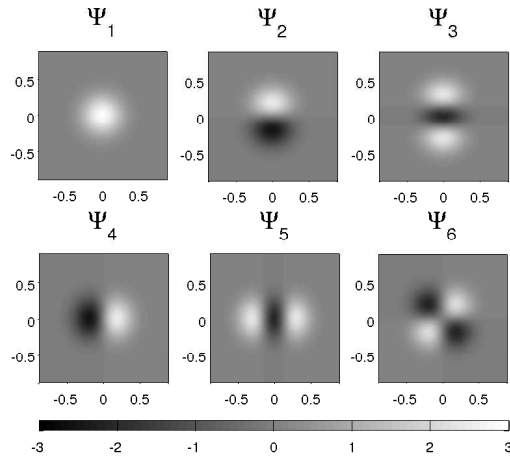


Figure 5. Normalized two-dimensional Gauss-Hermite basis used for the description of the leakage beam maps following Equation 13.

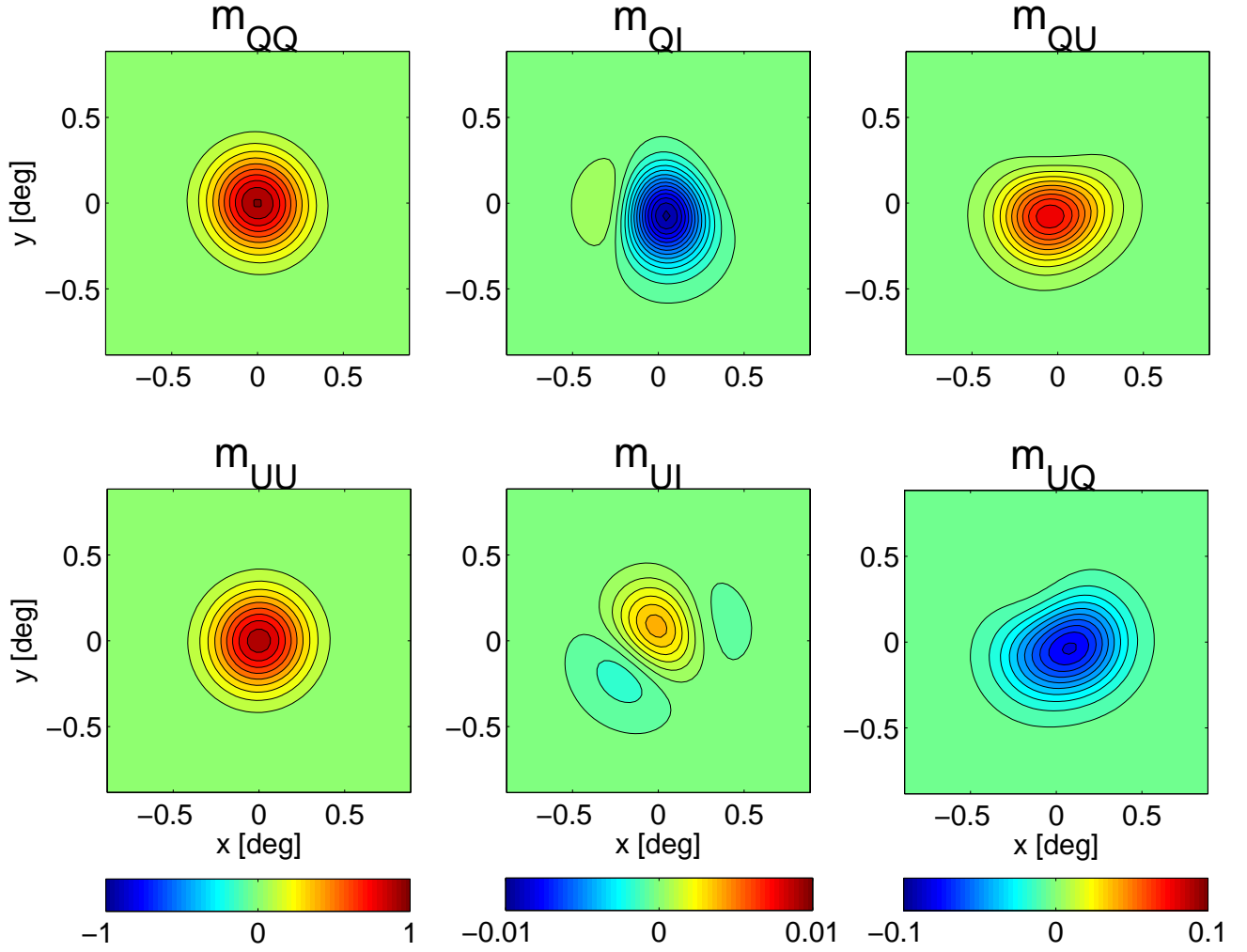


Figure 6. Mueller maps in instrumental coordinates generated by modelling the Tau A data with Equations 2 and 13 for main beams and leakage beams respectively. They represent the coupling of the different Stokes parameters (circular polarization V is predicted to be zero for CMB). The contour step for the m_{QQ} and m_{UU} maps is 0.1, for m_{QI} and m_{UI} it is 0.0007, and for m_{QU} and m_{UQ} it is 0.008. The relatively large m_{QU} and m_{UQ} fields are due to a known offset between the nominal instrument polarization angles as measured with the Moon and those measured with Tau A.